Journal of Materials Chemistry A

ROYAL SOCIETY OF CHEMISTRY

PAPER

View Article Online
View Journal | View Issue

Cite this: J. Mater. Chem. A, 2024, 12, 7058

A Mo–salicylaldehyde-linker (Mo–Tp) based 2D MOF as a single-atom catalyst for the nitrogen reduction reaction†

Hassan A. Alhadidi Almheiri, [ad] Nirpendra Singh, [bd] Dinesh Shetty, *[cd] Kyriaki Polychronopoulou [de] and Ali A. Alhammadi*[ad]

Received 31st October 2023
Accepted 2nd January 2024

DOI: 10.1039/d3ta06666e

rsc.li/materials-a

Two-dimensional (2D) materials for the electrocatalytic nitrogen reduction reaction (NRR) can offer a groundbreaking and sustainable alternative to the traditional Haber–Bosch process. Two-dimensional metal–organic frameworks (2D MOFs) have the potential to serve as single-atom catalysts (SACs), enabling the utilization of active metal centers up to 100% in the eNRR and also capable of reducing the HER effectively. This work outlines the screening of a new series of TM–Tp 2D MOFs (where Tp = 1,3,5-triformylphloroglucinol; TM = Cu, Ni, Cr, Mo, Os, Ru, and W) for the NRR, using density functional theory. Two screening stages based on the activation of the N_2 molecule and stabilization of the NNH intermediate showed that the Mo–Tp MOF monolayer is the most viable catalyst to be studied further. Mo–Tp shows outstanding stability and high potency towards being an efficient NRR catalyst with high selectivity. An investigation of the NRR pathway showed a limiting potential (U_L) of −0.38 V in the distal pathway. Furthermore, the theoretical faradaic efficiency (FE_t) is 100% towards the NRR. Our findings show that Mo-based 2D MOFs exhibit outstanding performance as NRR catalysts.

1 Introduction

The discovery of the Haber–Bosch process marks a pivotal moment in human history, enabling the large-scale production of ammonia (NH_3) from nitrogen gas (N_2). Evidently, NH_3 is the second highest-produced chemical worldwide finding applications in the production of fertilizers, chemicals, and pharmaceuticals.[1] Nevertheless, the Haber–Bosch process has significant drawbacks, requiring high temperatures (300–500 °C) and pressures (10–30 MPa).[1] In fact, it accounts for 1–2% of the global energy consumption, highlighting the pressing need for alternative approaches today.

The electrocatalytic nitrogen reduction reaction (NRR) has attracted a lot of research interest due to its ability to produce NH_3 under ambient conditions.[2] The NRR can harness renewable energy and transform NH_3 to an intermediate of energy storage eliminating the need for hydrogen (H_2) as an intermediary. However, the NRR suffers from incompetence due to the low faradaic efficiencies and competition coming from the parasitic hydrogen evolution reaction (HER).[3] In a recent review article by our group[4] the design criteria for efficient NRR catalysts have been critically discussed as well as experimental protocols that need to be followed for the validation of the reaction. Part of addressing NRR drawbacks is the investigation of the reaction mechanism with/without engaging isotopic studies and/or computational tools[4] over the most efficiently designed electrocatalysts.

Metal–organic frameworks (MOFs) have the potential to become efficient NRR catalysts because they have an active metal site surrounded by built-in tunable organic ligands.[4] Their applications in the NRR have yet to be fully exploited. The flexibility of metal-center variation and control over building block selection allows precision in targeting nitrogen activation in MOFs. Unfortunately, even the most porous MOFs face grand challenges of access to their active sites. One strategy to overcome these limitations involves harnessing reduced dimensionality within MOF systems by exfoliating a single monolayer[5] to expose the active sites and reduce the diffusion distance to reactants.

Two-dimensional (2D) MOFs are promising materials, compared with their bulk 3D MOFs because they exhibit enhanced electrical conductivity through conjugation, decreased electron transfer, and better exposure of the active

[a]Department of Chemical Engineering, Khalifa University of Science and Technology, P.O. Box 127788, Abu Dhabi, United Arab Emirates. E-mail: ali.aalhammadi@ku.ac.ae

[b]Department of Physics, Khalifa University of Science and Technology, P. O. Box 127788, Abu Dhabi, United Arab Emirates

[c]Department of Chemistry, Khalifa University of Science and Technology, P. O. Box 127788, Abu Dhabi, United Arab Emirates

[d]Center of Catalysis and Separation, Khalifa University of Science and Technology, Main Campus, Abu Dhabi, United Arab Emirates

[e]Mechanical Engineering Department, Khalifa University of Science and Technology, Main Campus, P.O. Box 127788, Abu Dhabi, United Arab Emirates

† Electronic supplementary information (ESI) available. See DOI: https://doi.org/10.1039/d3ta06666e

sites.[6,7] The tunability of 2D MOFs at the molecular level makes them excellent single atom catalysts (SACs) for the NRR.[7] Recently, a salicylaldehyde-based 2D MOF film was reported with unique coordination of the functional groups in a new series of copper-based 2D MOFs.[8] Moreover, they benefit through their scalability compared to other MOFs due to possessing an economical molecular building block.[8]

A plethora of metal centers (*e.g.* Ru, Pd… *etc.*) including molybdenum (Mo) have been advocated in literature as suitable NRR catalysts.[9] Mo atoms help promote NH_3 production naturally in biological nitrogenases.[9,10] Cui *et al.*[11] showed a $Mo_3(HAB)_2$ 2D MOF possessing a low limiting potential of −0.34 V. In a similar study conducted by Feng *et al.*,[12] a $Mo_3(C_2O)_{12}$ 2D MOF had given an almost similar value with a limiting potential of −0.36 V. The current understanding of how the coordination sphere affects reactivity through different frameworks is limited. It is of interest to investigate an asymmetric coordination sphere such as the one present in salicylaldehyde conjugated MOFs as a means of reducing nitrogen to ammonia.

We propose studying TM–Tp through density functional theory (DFT) computations to investigate different 2D transition metal (TM)–organic frameworks TM–Tp [TM = Cu, Ni, Cr, Mo, Os, Ru, and W; Tp = 1,3,5-triformylphloroglucinol] for the NRR. By investigating the ability of N_2 adsorption on MOFs and stabilizing the NNH intermediate, we show that Mo–Tp could be an efficient NRR catalyst. Previously studied Mo-based 2D MOFs have been the result of screened TM-MOF variations with their own screening procedures, such as TM = Co, Ni, Cu, and Mo[11] and TM = Sc–Au.[12] The limiting potential attained in our 2D Mo–Tp MOF is a competing one of −0.38 V. At most, this study could become a tremendous sequel to previously studied Mo-based 2D MOFs and help build a greater understanding of different organic ligands' roles during selective nitrogen-to-ammonia conversion.

1.1 Computational details

The DFT calculations were performed using the Vienna *ab initio* simulation package (VASP).[13] Van der Waals (vdW) interactions were considered using the DFT-D3 correction[14] in our spin-polarized calculations. The generalized gradient approximation (GGA) within the Perdew–Burke–Ernzerhof (PBE)[15] functional is used to express the exchange-correlation potential. The projected augmented wave (PAW)[16] method is used to describe ion–electron interactions with a cutoff energy of 500 eV. For bulk optimization calculations, a Monkhorst–Pack of 3 × 3 × 3 *k*-point mesh was used. A Monkhorst–Pack *k*-point mesh of 7 × 7 × 1 was employed for structural optimization and electronic properties of monolayers. Thermal stability of the Mo–Tp MOF structure was investigated using *ab initio* molecular dynamics (AIMD) with the canonical (NVT) ensemble.[17] The convergence of atomic forces and energy was set to 0.01 eV $Å^{-1}$ and 10^{-5} eV respectively. Additionally, a 15 Å vacuum space was added in the *z*-direction to avoid interactions between periodic images. For the band structure and density of states (DOS) calculations, DFT+*U* was used.[18] The crystal orbital Hamiltonian population (COHP) analysis was carried out using the Lobster package.[19] The VASPkit post-processing software was used to deal with electronic properties.[20] The VASPsol with an implicit solvation model was used to incorporate solvent effects.[21] Gibbs free energy calculations were calculated using the computational hydrogen electrode (CHE) model[22] {Note S1†}.

2 Results and discussion

2.1 Monolayer isolation from the bulk

The structure of bulk Cu–Tp[8] was used as a starting point for building other MOFs and used for further calculations after optimization. Fig. 1a shows the structure of the bulk Cu–Tp system after optimization. The experimental lattice parameters of the Cu–Tp MOF were $a = b = 14.5708$ Å and $c = 9.8014$ Å (ref. 8) whereas the DFT values changed to $a = b = 14.67286$ Å and $c = 9.70718$ Å. The cell volume and lattice parameters follow an increasing trend compared to that originally in the experiment. The rest of the TM–Tp bulk systems were optimized individually with varying lattice parameters outlined in Table S1.† The intrinsic pore diameter (D_{pore}) and interlayer distance (n) of each MOF system vary due to changes in the cell volume. However, all systems maintain a similar square planar coordination environment to the pristine Cu–Tp MOF film.[8]

In order to harness the actual benefits of reduced dimensions we consider an exfoliated monolayer in the rest of our DFT simulations. The exfoliation energies were computed as $[E_{(3\text{-layers})} - E_{(2\text{-layers})} + E_{(1\text{-layer})}]/A$, where $E_{(3\text{-layers})}$, $E_{(2\text{-layers})}$, and $E_{(1\text{-layer})}$ correspond to relaxed energies of 3 layers, 2 layers, and 1 layer of atoms respectively, and A is the exfoliation surface area of the unit cell. The exfoliation energies (E_{exf}) required to remove a single layer of TM–Tp from the bulk are outlined in Table S2† with ranges 13–44 meV $Å^{-2}$. The exfoliation energies are only slightly higher than that of graphene.[23] Fig. 1b shows the unit cell of the isolated monolayer of atoms. The coordination sphere around each atom is an asymmetric one with each metal atom surrounded by four oxygen atoms. The primitive cell contains an atomic formula of $TM_3(C_3O_2H)_6$.

Fig. 2a shows the energy levels of the d-band center of each TM–Tp MOF. The band energy levels are decomposed into spin-up (up) and spin-down (dn) states. As the energy level of the d-band center increases, the antibonding orbitals shift towards the Fermi level.[24] The d-band centers of Mo and Cr are located higher across the Fermi level than the other MOF systems. This is consistent with N_2 adsorption energies shown later in this work. Magnetism has been used intrinsically to tune the NRR activity of materials.[25] This is due to the possible formation of polarized charges around the metal sites which facilitate the activation of N_2 molecules. According to Hund's rule, many of the transition metals used in this work possess unfilled d-orbitals. The Ni–Tp MOF is nonmagnetic. The difference in the spin-up and spin-down energy states is causing magnetic moment in Cu, Cr, Mo, Os, Ru, and W in the TM–Tp MOFs. The calculated magnetic moments (μ_B) are summarized in Table S2.† Fig. S1† illustrates the band gap of different TM–Tp MOFs for both the bulk and monolayer. The simulated band gap of the Cu–Tp monolayer lies in the range of the experimental values,

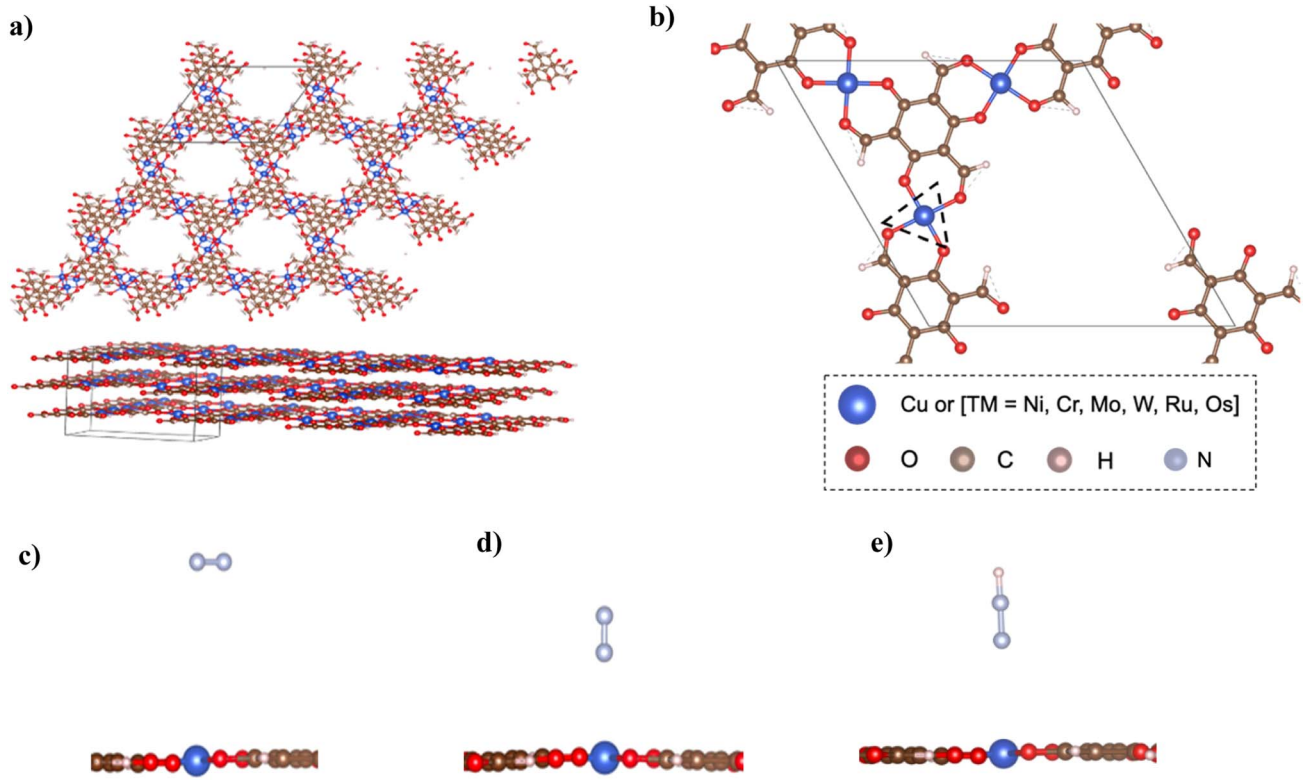

Fig. 1 (a) Cu–Tp bulk after optimization with lattice parameters $a = b = 14.67286$ Å and $c = 9.70718$ Å. (b) Unit cell of Cu–Tp {the dotted triangle denotes the N_2 adsorption location} [blue: TM; brown: C; red: O; pink: H; cyan: N]. (c) Side-on configuration of the N_2 molecule on the Cu–Tp MOF monolayer. (d) End-on configuration of the N_2 molecule on the Cu–Tp MOF monolayer. (e) The *NNH intermediate adsorbed in the end-on configuration on the Cu–Tp MOF monolayer.

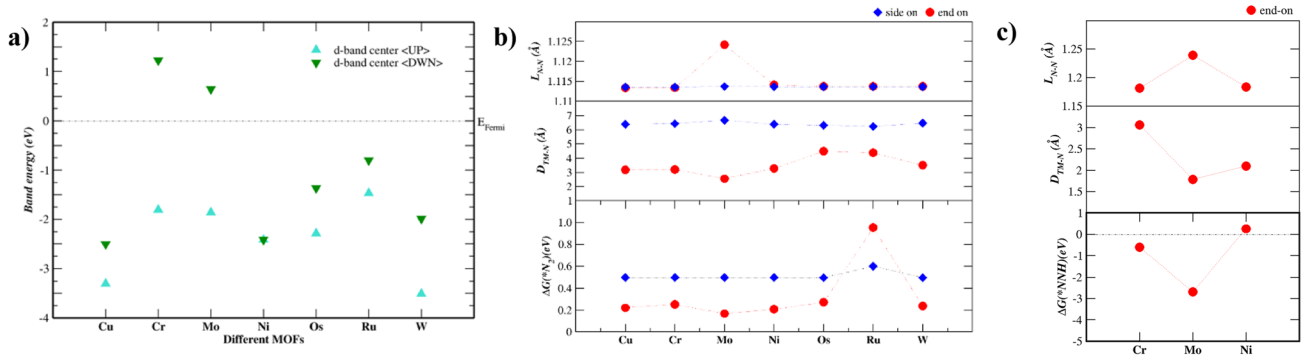

Fig. 2 (a) Energy levels of the d-band center in each TM–Tp MOF monolayer system [TM = Cu, Ni, Cr, Mo, Os, Ru, and W] decomposed into spin-up (UP) and spin-down (DOWN) states. (b) The first screening step consisting of the adsorption free energy of N_2 {$\Delta G(*N_2)$}, the distance between the transition metal (TM) and nearest N atom {D_{TM-N}}, and the N–N bond length {L_{N-N}} for our *N_2/TM–Tp MOF systems (c) the second screening step consisting of the adsorption free energy of the NNH intermediate {$\Delta G(*NNH)$}, the distance between the transition metal (TM) and nearest N atom {D_{TM-N}}, and the N–N bond length {L_{N-N}} for our *NHH/TM–Tp MOF systems.

which is 1.6 eV for Cu–Tp.[8] The electronic bandgaps increase in monolayers due to quantum confinement.[26]

2.2 Screening favorable TM–Tp 2D MOFs for the NRR

Accordingly, we screen NRR electrocatalysts based on their ability to adsorb N_2 (ΔG_{N_2}) as a first screening layer and the ability to stabilize the NNH intermediate as a second screening layer. These activity descriptors are proposed based on the two most possible potential limiting steps (PLS).[26–31] Moreover, Nørskov *et al.*[27,30] showed that the adsorption energy of N_2 scales with the rest of the intermediate adsorption energies.

The metal active center is usually the active site for the NRR. In our investigation, we consider the metal active centre for N_2 adsorption. The side-on and end-on configurations are considered, as shown in Fig. 1c and d, respectively. The reaction step $N_2 + * \Rightarrow *N_2$ is investigated as the first screening step, as

shown in Fig. 2b. None of the TM–Tp (TM = Cu, Ni, Cr, Mo, Os, Ru, and W) systems can adsorb nitrogen spontaneously. Mo–Tp possessed the lowest value of ΔG_{N_2} of 0.17 eV; Ni–Tp, Cu–Tp, and Cr–Tp come after that with free energies of adsorption of 0.20 eV, 0.22 eV, and 0.25 eV, respectively. Only Mo–Tp, Ni–Tp, and Cr–Tp proceed to the next stage of the screening process. Selecting Cr–Tp was done instead of Cu–Tp because of the higher energy level occupied by the d-band center.

The stabilization of the NNH intermediate is used as a second step to screen the remaining possible NRR catalysts. The configuration of the NNH intermediate depends on the prior adsorption of the N_2 molecule, in our case, we have worked with the end-on configuration of NNH shown in Fig. 1e. The reaction in the first protonation step of N_2 is $*N_2 + H^+ + e^- \Rightarrow *NNH$. The TM–Tp MOF possessing the lowest value of ΔG_{NNH} was Mo–Tp with a free energy of −2.68 eV in Fig. 2c. Additionally, the N–N bond distance (L_{N-N}) elongates to 1.24 Å and the distance between Mo and N is 1.78 Å. We proceed to investigate Mo–Tp with the N_2 molecule in the end-on configuration.

2.3 Stability and electronic structure of Mo–Tp

Having exceptional stability is required for using 2D MOFs as possible NRR electrocatalysts. Mo–Tp has a lattice constant $a = b = 15.12$ Å, which is slightly larger than that of the Cu–Tp MOF ($a = b = 14.57$ Å).[8] The Mo–O bond length is 2.06 Å and the diameter of each pore (D_{pore}) is of 13.74 Å. Structural stability is assessed *via* calculating the cohesive formation energy of the Mo–Tp MOF monolayer. The required binding energy per metallic atom was evaluated for the Mo–Tp monolayer using the equation $E_b = [E_{tot} - E_{ligand} - E_{Mo}]/3$; E_{tot}, E_{ligand}, E_{Mo} are the total energy of the unit cell, the energy of an isolated organic ligand, and the energy of an isolated Mo atom respectively. The magnitude of the binding energy (E_b) is −9.24 eV, which is comparable to that of other Mo-based 2D MOFs studied computationally.[11,12]

Thermal stability of the Mo–Tp monolayer is checked using *ab initio* molecular dynamics (AIMD) in the NVT ensemble at 300 K, 500 K, and 1000 K and for different simulation times (Fig. S2–S4†). Fig. S2† shows the top and side views of the Mo–Tp structure after an AIMD run at 500 K and 2500 fs. There is neither significant distortion of the Mo–Tp monolayer nor was there a breakage of the Mo–O bond at 300 K (Fig. S2†), 500 K (Fig. S2†), and 1000 K (Fig. S3†). Moreover, the energy fluctuations at different temperatures are almost imperceptible meaning no lower-level structures were present during the AIMD runs. Temperatures as high as 1000 K will most likely not be reached due to MOFs getting pyrolyzed. Yet, it is assuring that theoretically the Mo–Tp monolayer possesses excellent thermodynamic stability under different conditions.

The Mo–Tp monolayer has a magnetic moment of $12.0\mu_B$ and is mainly due to the Mo-atoms. The spin-polarized energy difference was computed through $\Delta E_{spin} = E_{magnetic} - E_{non\text{-}magnetic}$, where $E_{magnetic}$ and $E_{non\text{-}magnetic}$ are the energies of the magnetic states and the non-magnetic states, respectively. The magnitude of the spin energy is −1.89 eV which is comparable to that on Mo atoms from reported work.[11]

The electronic structure of Mo–Tp was studied through the total density of states (TDOS) and projected density of states (PDOS) of Mo, C, O and H in Fig. 3a and S5.† The asymmetry in the DOS leads to the magnetism in our material. The e_g orbitals are present at a higher energy level than the t_{2g} orbitals, consistent with crystal field theory.[32] The magnetism of Mo–Tp can be related to the asymmetry of the spin-up and spin-down states.[33] Moreover, the charge density difference in Fig. 4a and the crystal orbital Hamiltonian population (COHP) in Fig. 3b show that bonding is a result of the charge donation from Mo-d orbitals to the O-p_z orbitals. However C and O interact through their p_z orbitals as shown in the DOS in Fig. S5.†

A uniform distribution of charges is observed in our Mo–Tp conjugated MOF through the charge density distribution (CDD) in Fig. 4b and the electron localization function (ELF) mapping in Fig. 3f. In Table S6† we demonstrate through a charge analysis that Mo loses a charge of 1.40*e* while O atoms gain a charge of 1.13*e*. The Mo atom gains a slight positive charge due to charge donation, making it a suitable site for N_2 activation. Finally, the electronic structure was studied by plotting the band structure of the spin-up and spin-down states in Fig. 3c. A semi-conducting behaviour of the material was observed, featuring a smaller bandgap in the spin-up states than the spin-down states. A small bandgap value ensures that charge can be donated to the adsorbate species at ease throughout the reaction process.

2.4 Adsorption of the N_2 molecule on Mo–Tp

The end-on N_2 adsorption is shown in Fig. 4d. The overlap of Mo and N_2 states is sufficient to transfer charges between the Mo atom to N_2. This claim is supported by the charge density difference (CDD) in Fig. 4e where the Mo atom transfers 0.14*e* charge to weaken the N_2 bond. Charge accumulates on the edges of the N atom allowing it to be easily hydrogenated. The equivalent occurs for depletion (blue) of charges which helps weaken the N_2 triple bond. This proves that Mo is able to activate the N_2 bond, as shown in previous experimental studies.[34]

The density of states (DOS) and COHP plots in Fig. 3d and e were analysed to uncover the shift of electronic states in the N_2/Mo–Tp monolayer system. The pDOS of adsorbed N_2 ($*N_2$) shows that the states are shifted lower across the Fermi level in a sense of strengthening the Mo–N bond. A weak overlap of the bonding states is initially observed in the pCOHP analysis between Mo and the nearest N atom. This can be quantitatively assessed through the Mulliken gross orbital population (GP) and −ICOHP values. The ELF mapping of the N_2/Mo–Tp system is shown in Fig. 3g. Mulliken GP values in Mo are dominant *via* the $4d_{yz}$ and $4d_{x^2}$–d_{y^2} orbitals, making them the most likely orbitals that hold electrons participating in the charge donation process.

As the NRR progresses, Mo starts to interact with the first N atom. In Fig. S6,† the pCOHP plot of *NNH is shown. The −ICOHP values increase from 1.21 and 1.24 eV per bond to 4.45 and 4.55 eV per bond for the first and second spin channels respectively. This conforms to the strong bonding facilitating between Mo and N during *NNH formation allowing further hydrogenation.

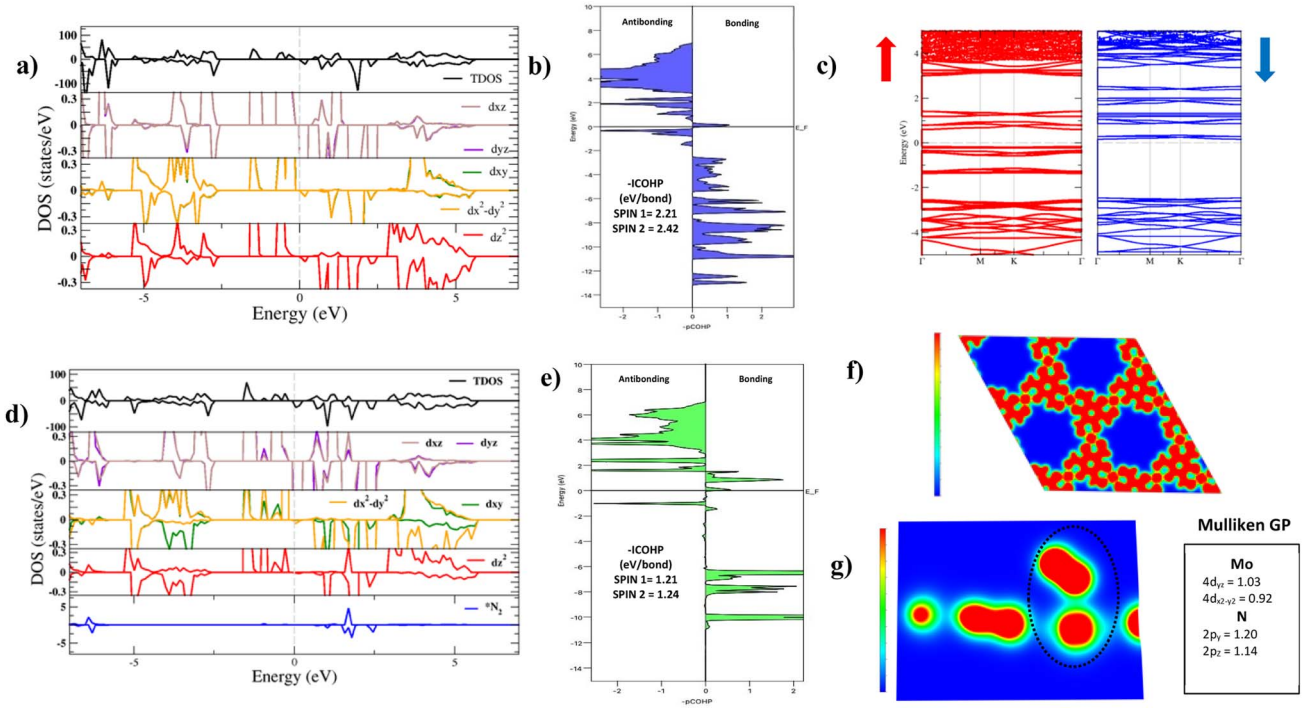

Fig. 3 (a) Density of states plot showing the total density of states (TDOS) and projected density of states (pDOS) of Mo, C, O, and H in our Mo–Tp MOF monolayer. (b) Projected crystal orbital Hamiltonian population (pCOHP) between Mo and the nearest O atom. (c) Band structure of the Mo–Tp MOF monolayer decomposed into spin-up (red) and spin-down (blue) states. (d) Density of states plot showing the total density of states (TDOS) and projected density of states (pDOS) of Mo, C, O, H and N in the $*N_2$/Mo–Tp MOF system. (e) Projected crystal orbital Hamiltonian population (pCOHP) between Mo and the nearest N atom in N_2. Electron localization function (ELF) mapping of (f) the Mo–Tp MOF monolayer. (g) The $*N_2$/Mo–Tp MOF system in the *z*-axis with the dominant Mulliken orbital gross population (GP) values.

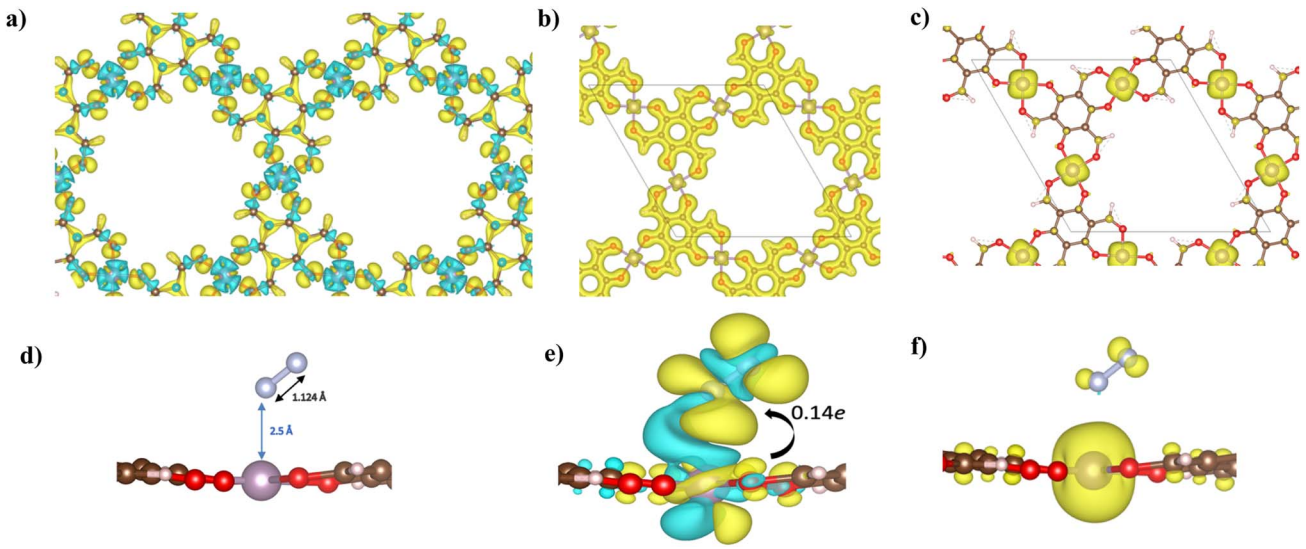

Fig. 4 (a) Charge density difference, (b) charge density distribution (CDD), and (c) spin density of the Mo–Tp MOF monolayer. (d) Top view of the optimized structure of the adsorbed N_2/Mo–Tp MOF monolayer system. (e) Total charge density difference. (f) Spin density of the $*N_2$/Mo–Tp MOF monolayer system. Charge accumulation (+) is shown in yellow while charge depletion (–) is in blue. Similarly, spin-up density is shown in yellow while spin-down density is in blue. Isosurfaces are set to 0.10 a.u.

The magnetic state of Mo–Tp shifts from $12.00\mu_B$ to $11.994\mu_B$ after N_2 adsorption. This indicates that some of the uncoupled electrons contributing to the overall spin have taken part in the bonding process between N_2 and Mo. Moreover, the spin density diagrams shown in Fig. 4f indicate spin density change as N_2 adsorbs. The depletion of the spin density on the N atom

closer to Mo signifies the beginning of a bond formation between Mo and N.[35]

2.5 Performance of Mo–Tp towards the NRR

Fig. S8† shows alternating and distal mechanisms and their intermediates studied for the Mo–Tp monolayer. The bonding between intermediates and the Mo-atom provides evidence that it is the active site for the NRR. In the alternating mechanism, the N–N bond is broken through the protonation of alternate N atoms successively. Finally, two NH_3 molecules are released in succession. The distal mechanism proceeds with the protonation of only one N atom at a time. The N atom located at the further end is first released as NH_3, after which the remaining N atom is hydrogenated again until it leaves the surface as an NH_3 molecule.

The free energy NRR diagrams for both the alternating and distal mechanisms are depicted in Fig. 5a and b, respectively. The first step of N_2 adsorption is the same for both mechanisms. The free energy of N_2 adsorption is uphill by 0.17 eV with a reaction step $N_2 + * \Rightarrow *N_2$; where "*" refers to being adsorbed on Mo–Tp. Following that is the first hydrogenation step, common for the two mechanisms. The NNH intermediate forms spontaneously with a downhill free energy of 2.854 eV in the reaction step $*N_2 + H^+ + e^- \Rightarrow *NNH$. The following reaction steps consist of different intermediates for the distal and alternating pathways.

The potential limiting step for the alternating mechanism consists of hydrogenating the NNH intermediate into NHNH. This step has the largest uphill free energy change ΔG_{NHNH} with 0.53 eV for the reaction $*NNH + H^+ + e^- \Rightarrow *NHNH$. Thus, it sets the limiting potential (U_L) for the alternating mechanism as −0.53 V. Next, the free energy change ΔG_{NHNHH} of the reaction step $*NHNH + H^+ + e^- \Rightarrow *NHNH_2$ is downhill by 0.31 eV. Following that is the reaction $*NHNH_2 + H^+ + e^- \Rightarrow *NH_2NH_2$ with an uphill free energy change ΔG_{NHHNHH} of 0.15 eV. The first NH_3 molecule is released during the reaction $*NH_2NH_2 + H^+ + e^- \Rightarrow *NH_2NH_3$ with a downhill free energy change $\Delta G_{NHHNHHH}$ of 0.23 eV. Finally, the second NH_3 molecule is formed and released from the Mo–Tp surface with a minor uphill free energy change $\Delta G_{*NH_3} = 0.016$ eV in the corresponding reaction step $*NH_2 + H^+ + e^- \Rightarrow *NH_3$.

The potential limiting step for the distal mechanism is the formation of NNHH from the NNH intermediate. This step is the highest uphill distal free energy change ΔG_{*NNHH} by 0.38 eV for the reaction $*NNH + H^+ + e^- \Rightarrow *NNHH$. It sets the limiting potential (U_L) for the distal mechanism as −0.38 V. Next, the free energy change ΔG_{*NNHHH} of the formation step $*NNHH + H^+ + e^- \Rightarrow *NNH_3$ is downhill by 0.53 eV. This is also where the first NH_3 molecule forms and leaves the remaining N atom on the Mo–Tp surface. Protons then attach to the remaining N atom with an uphill free energy change ΔG_{*NH} of 0.043 eV in the reaction step $*NNH_3 + H^+ + e^- \Rightarrow *NH + NH_3$. Following that is the reaction step $*NH + H^+ + e^- \Rightarrow *NH_2$ with an uphill free energy change ΔG_{NHH} of 0.097 eV. Finally, the second NH_3 molecule forms during the reaction $*NH_2 + H^+ + e^- \Rightarrow *NH_3$ with an uphill free energy change ΔG_{*NHHH} of 0.17 eV. The desorption of NH_3 from the Mo–Tp surface occurs similarly for both the distal and alternating mechanisms. The free energy change corresponding to the desorption of ammonia ΔG_{NHHH} is slightly uphill by 0.009 eV with the reaction step $*NH_3 \Rightarrow NH_3 + *$. This means the active sites free up more N_2 molecules to form ammonia.

The lowest limiting potential (U_L) is at a value of −0.38 V and corresponds to the distal mechanism. Therefore, the path that the NRR would proceed in to form ammonia is *via* the distal mechanism. The overpotential (η) can be computed using the equation $\eta = U_{eq} - U_L$, where U_{eq} corresponds to the equilibrium potential for the NRR and is at a constant value of −0.16 V according to Zhao *et al.*[36] We consider a U_L value of −0.38 V and obtain an overpotential of 0.22 V. Considering some of the Mo-based NRR catalysts[36–46] and other benchmark NRR catalysts[35,47–59] with limiting potentials $U_L = [-0.35 \Leftrightarrow -0.71$, the Mo–Tp monolayer is considered one of the best catalysts for the NRR. It shows similar proficiency towards being a good NRR catalyst to the other Mo-based 2D MOFs.[11,12]

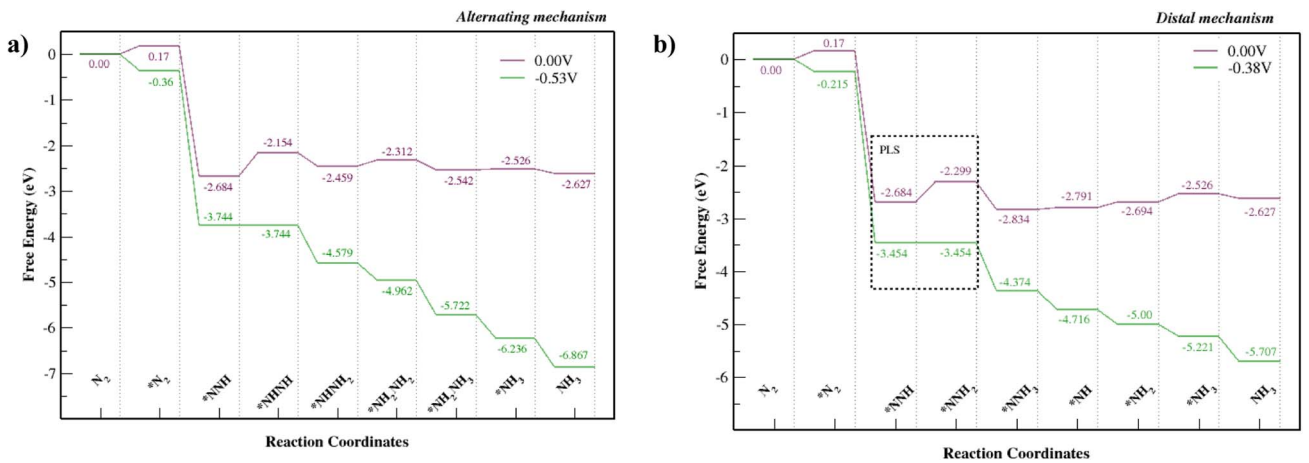

Fig. 5 NRR free energy diagrams for the (a) alternating mechanism and (b) the distal mechanism, where * denotes being adsorbed on Mo–Tp MOF.

2.6 Analysis of selectivity

The greatest challenge faced by NRR catalysts is the parasitic HER.[3] A selectivity analysis needs to be carried out on the competitive adsorption process between nitrogen and the hydrogen proton. The Mo–Tp MOF monolayer consists of an additional O–CH group which could bring in H protons due to forces of hydrogen bonding. Therefore, we have considered three possible adsorption sites: the Mo atom, the carbon atom in the O–CH group (C1), and the carbon atom not connected to the O–CH group (C2) shown in Fig. S9a.†

The free energy difference $[\Delta G_{*H} - \Delta G_{*N_2}]$ can be used to study the competitive adsorption of *H protons and N_2,[60] thus addressing the selectivity of the Mo–Tp monolayer MOF. Values of $[\Delta G_{*H} - \Delta G_{*N_2}]$ are summarized in Table S9† for adsorption sites Mo, C1, and C2. Accordingly, ΔG_{*H} is the free energy of H adsorption and ΔG_{*N_2} is the free energy of N_2 adsorption. The metal centre Mo is the main adsorption site for the NRR, which shows to be very selective for N_2 adsorption due to having a positive $[\Delta G_{*H} - \Delta G_{*N_2}]$ value of 0.36 eV. However, the C1 and C2 adsorption sites are more selective towards H adsorption with $[\Delta G_{*H} - \Delta G_{*N_2}]$ values of −0.113 eV and −0.241 eV respectively. The Mo site could adsorb N_2 while the C1 and C2 sites could ensure that there is a good supply of protons for the reaction.

The selectivity of Mo–Tp can be attributed to the shift of its magnetic states with the adsorption process. The magnetic moment increases from $12.00\mu_B$ to $13.00\mu_B$ as the H proton adsorbs. Fig. S9b† shows the spin density diagram consisting of a top and side view. An increase in the magnetic moment comes from unpaired electrons between Mo–Tp and the H proton. Unlike N_2, the spin density surrounding the H proton does not decrease. This is due to the impairment of spins featuring the electrons surrounding the two atoms. Therefore, the Mo atom should be highly selective towards N_2 adsorption.

The theoretical faradaic efficiency (FE_t) was estimated through the Boltzmann distribution. Its value can be obtained using the formula $FE_t = \{1/(1 + \exp(-[\Delta G_{*H} - \Delta G_{*N_2}]/k_BT))\}$, where k_BT is the product of the Boltzmann constant (k_B) and temperature ($T = 300$ K).[38] The calculated faradaic efficiency was 100% for the Mo–Tp MOF which is an excellent value agreeing with previous Mo-based 2D MOFs.[11]

2.7 Magnetic and charge variation across intermediates and Mo–Tp moieties

Previous work[11] suggests that intuition on the NRR catalytic process can be developed by analysing the intermediate N–N bond lengths, distance between Mo and the nearest N atom, Bader charge analysis, and the magnetic moment variation of the NRR intermediates. These are summarized in Fig. 6 and Table S6.† The elongation and eventual cleavage of the N–N bond can be observed through monitoring the N–N bond distance (L_{N-N}) in Fig. 6a and b for the distal and alternating mechanisms respectively. The bond stretches in the distal mechanism and finally ruptures during the *N···NHHH step, while in the alternating mechanism the bond ruptures during the *NHH···NHHH step. Mo–Tp is able to steadily break the N–N triple bond in both mechanisms, showing that it could be an efficient NRR catalyst.[61,62]

The intermediates have to be brought close enough to the Mo atom to complete the NRR without them escaping the surface. The distance between the Mo atom and the nearest N atom in intermediates was monitored throughout the course of the reactions; this is shown in Fig. 6c and d for the distal and alternating mechanisms respectively. In both mechanisms, N_2 adsorbs at 2.56 Å from the surface. The intermediates are then brought closer to the surface at Mo–N distances 2.00–1.50 Å. Finally, the *NHHH intermediate is pushed away from the surface at the end of the reaction with a Mo–N distance of 3.1 Å.

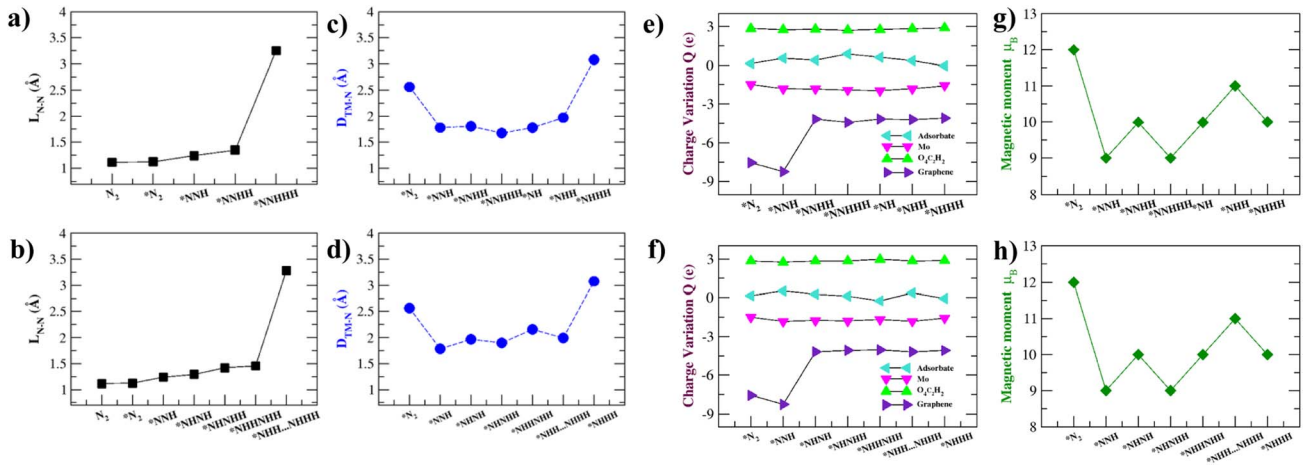

Fig. 6 N–N bond length (L_{N-N}) in Å throughout the (a) distal mechanism and the (b) alternating mechanism. The distance between Mo (TM) and the nearest N atom across all intermediates in Å for the (c) distal mechanism and (d) alternating mechanism. Charge variation in intermediates by Bader charge analysis of the adsorbate, Mo, $O_4C_2H_2$, and graphene moieties across the (e) distal mechanism and (f) alternating mechanism. Magnetic moment variation of intermediates across the (g) distal mechanism and (h) alternating mechanism, where * denotes being adsorbed on Mo–Tp MOF.

This ensures that the NH_3 product easily leaves the surface of Mo–Tp after completing the reaction.[63]

To study the process of charge transfer a Bader charge analysis was carried out. On average, charge depletes from the Mo atom to force the completion of the NRR. The Mo–Tp MOF charge transfer is studied based on moieties, including that of the adsorbate, Mo atom, $O_4C_2H_2$, and graphene. The results are summarized in Fig. 6e and f and Table S6† for the distal and alternating mechanisms respectively. As N_2 adsorbs, it gains a charge of 0.14*e*. Meanwhile, the Mo atom depletes 1.50*e* and gains a net positive charge. Graphene supplies charges by depleting 7.56*e* amounts of charge. $O_4C_2H_2$ linkers around the Mo atom accumulate 2.84*e*. As for the rest of the intermediates, the adsorbates accumulate charges in the range of 0.128–0.87*e*. Similarly, the Mo atom depletes 1.55–1.97*e*, the $O_4C_2H_2$ linkers accumulate 2.71–2.98*e*, and graphene depletes 4.04–8.26*e* charge. The catalytic activity of the Mo–Tp MOF monolayer comes from the charge transfer between Mo and adsorbate moieties.

Variations in magnetism are used to designate the ground states of different NRR intermediates. Fig. 6g and f show the changes in magnetic moment (μ_B) for the distal and alternating mechanisms respectively. Clearly seen is that the magnetic moment decreases as the reaction proceeds. The spin density is highly localized around the Mo atom for all intermediates (Fig. S7†) and decreases somewhat because of charge transfer. Localization of spin is critical to having an efficient NRR process as observed with some of the different catalysts.[64]

3 Conclusions

In conclusion, we have used density functional theory (DFT) calculations to analyse a TM–Tp 2D MOF [TM = Cu, Ni, Cr, Mo, Os, Ru, and W; Tp = 1,3,5-triformylphloroglucinol] as a single-atom catalyst for the NRR. We begin by isolating a single layer of atoms from the bulk, from which 2D MOFs are likely to be synthesized. Through using current state-of-the-art screening methods featuring the ability of the MOF systems to adsorb N_2 and stabilize the NNH intermediate, we isolate Mo–Tp as an NRR catalyst to focus on. Moreover, we provide evidence of outstanding stability and NRR catalytic activity of Mo–Tp. The potential limiting step (PLS) $*NNH + H^+ + e^- \Rightarrow *NNHH$ sets the limiting potential (U_L) for the distal mechanism as −0.38 V. Moreover, it shows a 100% theoretical faradaic efficiency (FE_t) towards the NRR. Mo–Tp shows great promise as an efficient NRR catalyst and is able to exploit the uniqueness of the salicylaldehyde linkers. This could introduce the prospective of Mo-based 2D MOFs with various linkers for future applications in the NRR.

Conflicts of interest

The authors declare no conflicts of interest.

Acknowledgements

The authors would like to acknowledge the contribution of Khalifa University's high-performance research computing and research computing facilities and the Center of Catalysts and Separations (CeCaS) through the Khalifa University grant RC2-2018-024 to the results of this research. N. S. acknowledges the financial support from Khalifa University of Science and Technology under the Research Innovation grant (RIG-2023-01). We would like to acknowledge Zhen Feng for sharing his DFT input for us to build on. Finally, we would like to acknowledge Dr Sharmarke Mohammed and Dr Khalid Al Ali for their fruitful discussions towards this project.

References

1 C. Tang and S. Z. Qiao, *Chem. Soc. Rev.*, 2019, **48**, 3166–3180.
2 X. Guo, H. Du, F. Qu and J. Li, *J. Mater. Chem. A*, 2019, **7**, 3531–3543.
3 S. L. Foster, *Nat. Catal.*, 2018, **7**, 490–500.
4 S. Singh, A. K. Mohammed, A. A. AlHammadi, D. Shetty and K. Polychronopoulou, *Int. J. Hydrogen Energy*, 2023, **48**, 34700–34739.
5 L. Xiao, Z. Wang and J. Guan, *Coord. Chem. Rev.*, 2022, **472**, 214777.
6 Y. Wang, Q. Li, W. Shi and P. Cheng, *Chin. Chem. Lett.*, 2020, **7**, 1768–1772.
7 Y. Pang, C. Su, G. Jia, L. Xu and Z. Shao, *Chem. Soc. Rev.*, 2021, **50**, 12744–12787.
8 A. K. Mohammed, *Chem. Commun.*, 2023, **59**, 2608–2611.
9 K. Danyal, D. R. Dean, B. M. Hoffman and L. C. Seefeldt, *Biochemistry*, 2011, **50**, 9255–9263.
10 S. L. Foster, S. I. P. Bakovic and R. D. Duda, *Nat. Catal.*, 2018, **1**, 490–500.
11 Q. Cui, G. Qin, W. Wang, K. R. Geethalakshmi, A. Du and Q. Sun, *J. Mater. Chem. A*, 2019, **7**, 14510–14518.
12 Z. Feng, Z. Yang, X. Meng, F. Li, Z. Guo, S. Zheng, G. Su, Y. Ma, Y. Tang and X. Dai, *J. Mater. Chem. A*, 2022, **10**, 4731–4738.
13 G. Kresse and J. Furthmüller, *Comput. Mater. Sci.*, 1996, **6**, 15–50.
14 S. Grimme, J. Antony, S. Ehrlich and H. Krieg, *J. Chem. Phys.*, 2010, **132**, 154104.
15 J. P. Perdew, K. Burke and M. Ernzerhof, *Phys. Rev. Lett.*, 1996, **77**, 3865–3868.
16 G. Kresse, *Phys. Rev. B: Condens. Matter Mater. Phys.*, 1999, **59**, 1758–1775.
17 G. J. Martyna, M. L. Klein and M. Tuckerman, *J. Chem. Phys.*, 1992, **97**, 2635–2643.
18 B. Himmetoglu, A. Floris, S. de Gironcoli and M. Cococcioni, *Int. J. Quantum Chem.*, 2014, **114**, 14–49.
19 S. Maintz, V. L. Deringer, A. L. Tchougreeff and R. Dronskowski, *J. Comput. Chem.*, 2016, **37**, 1030–1035.
20 V. Wang, N. Xu, J. C. Liu, G. Tang and W. T. Geng, *Comput. Phys. Commun.*, 2021, **267**, 108033.
21 K. Mathew, R. Sundararaman, K. Letchworth-Weaver, T. A. Arias and R. G. Hennig, *Chem. Phys.*, 2014, **140**, 084106.
22 J. K. Nørskov, *J. Phys. Chem. B*, 2004, **108**, 17886–17892.
23 J. H. Jung, C.-H. Park and J. Ihm, *Nano Lett.*, 2018, **18**, 2759–2765.

24 B. Hammer and J. K. Nørskov, *Adv. Catal.*, 2000, **45**, 71–129.
25 X. Guo and S. Huang, *Electrochim. Acta*, 2018, **284**, 392–399.
26 A. Chaves, *npj 2D Mater. Appl.*, 2020, **4**, 29.
27 T. Bligaard, J. K. Nørskov, S. Dahl, J. Matthiesen, C. H. Christensen and J. Sehested, *J. Catal.*, 2004, **224**, 206–217.
28 J. K. Nørskov, *J. Catal.*, 2002, **209**, 275–278.
29 C. J. H. Jacobsen, S. Dahl, B. G. S. Clausen, S. Bahn, A. Logadottir and J. K. Nørskov, *J. Am. Chem. Soc.*, 2001, **123**, 8404–8405.
30 J. K. Nørskov, T. Bligaard, B. Hvolbæk, F. Abild-Pedersen, I. Chorkendorff and C. H. Christensen, *Chem. Soc. Rev.*, 2008, **37**, 2163–2171.
31 E. Skúlason, *Phys. Chem. Chem. Phys.*, 2012, **14**, 1235–1245.
32 T. Wolfram and Ş. Ellialtıoğlu, *Crystal Field Theory*, Cambridge University Press, Cambridge, 2014, pp. 90–122.
33 I. Garg, H. Sharma, N. Kapila, K. Dharamvir and V. K. Jindal, *Nanoscale*, 2011, **3**, 217–224.
34 M. Arif, *Chem. Eng. J.*, 2023, **451**, 138320.
35 C. Fang and W. An, *Nano Res.*, 2021, **14**, 4211–4219.
36 J. Zhao and Z. Chen, *J. Am. Chem. Soc.*, 2017, **139**, 12480–12487.
37 W. Zhao, L. Chen, W. Zhang and J. Yang, *J. Mater. Chem. A*, 2021, **9**, 6547–6554.
38 X. Zhang, T. Zhao, L. Yan and Z. Su, *Phys. Chem. Chem. Phys.*, 2023, **25**, 12371–12378.
39 L. Gao, *J. Mater. Chem. A*, 2019, **7**, 19838–19845.
40 X. Li, T. Li and Y. Ma, *Adv. Energy Mater.*, 2018, **8**, 1801357.
41 L. Zhang, X. Ji and X. Ren, *Adv. Mater.*, 2018, **30**, 1800191.
42 X. Ren, J. Zhao and Q. Wei, *ACS Cent. Sci.*, 2019, **5**, 116–121.
43 H. Cheng, L. Xin Ding and G. Feng Chen, *Adv. Mater.*, 2018, **30**, 1803694.
44 J. Zhao and Z. Chen, *J. Am. Chem. Soc.*, 2017, **139**, 12480–12487.
45 L. Hui, Y. Xue and H. Yu, *J. Am. Chem. Soc.*, 2019, **141**, 10677–10683.
46 H. Niu, X. Wang and C. Shao, *ACS Sustain. Chem. Eng.*, 2020, **8**, 13749–13758.
47 J. G. Howalt, T. Bligaard, J. Rossmeisl and T. Vegge, *Phys. Chem. Chem. Phys.*, 2013, **15**, 7785–7795.
48 X. Wang, Q. Zhang, W. Hao, C. Fang, J. Zhou and J. Xu, *J. Mater. Chem. A*, 2022, **10**, 15036–15050.
49 A. Rasool, I. Anis, S. A. Bhat and M. A. Dar, *Phys. Chem. Chem. Phys.*, 2023, **25**, 22275–22285.
50 Y. Ling, *J. Mater. Chem. A*, 2020, 12996–13003.
51 Z. Feng, Y. Tang and W. Chen, *Phys. Chem. Chem. Phys.*, 2020, **22**, 9216–9224.
52 Z. Geng, Y. Liu and X. Kong, *Adv. Mater.*, 2018, **30**, 1803498.
53 D. Ma, Z. Zeng and L. Liu, *J. Phys. Chem. C*, 2019, **123**, 19066–19076.
54 J. Han, Z. Liu and Y. Ma, *Nano Energy*, 2018, **52**, 52264–52270.
55 Y. Cao, Y. Gao and H. Zhou, *Adv. Theory Simul.*, 2018, **1**, 1800018.
56 D. Ma, Z. Zeng and L. Liu, *J. Energy Chem.*, 2021, **54**, 501–509.
57 H. Zou, W. Rong and S. Wei, *Proc. Natl. Acad. Sci. U.S.A.*, 2020, **117**, 29462–29468.
58 H. Yu, Y. Xue and L. Hui, *Natl. Sci. Rev.*, 2021, **8**, nwaa213.
59 R. Hao, W. Sun and Q. Liu, *Small*, 2020, 2000015.
60 C. Choi, S. Back, N. Y. Kim, J. Lim, Y. H. Kim and Y. Jung, *ACS Catal.*, 2018, **8**, 7517–7525.
61 L. Shi, Y. Yin, S. Wang and H. Sun, *ACS Catal.*, 2020, **10**, 6870–6899.
62 W. Guo, K. Zhang, Z. Liang, R. Zou and Q. Xu, *Chem. Soc. Rev.*, 2019, **48**, 5658–5716.
63 J. Wan, J. Zheng, H. Zhang, A. Wu and X. Li, *Catal.: Sci. Technol.*, 2022, **12**, 38–56.
64 Y. Zhang, *J. Mater. Chem. A*, 2022, **10**, 23704–23711.